

Mechanical behavior in liquid lead of Al₂O₃ coated 15-15Ti steel and an Alumina-Forming Austenitic steel designed to mitigate their corrosion

Ingrid Proriol Serre and Jean-Bernard Vogt

Univ.Lille, CNRS, INRAE, Centrale Lille, UMR 8207, UMET, Unité Matériaux et Transformations, 59000 Lille, France

Corresponding author: Ingrid PRORIOL SERRE: Ingrid.proriol-serre@univ-lille.fr

Highlights

No LME by liquid lead at 400 °C and 500 °C of the Al₂O₃ coated 15-15Ti steel.

LME at 500 °C of the studied AFA steel

Intergranular cracking of the AFA steel at 500 °C in presence of liquid lead - grain boundary wetting-dominated LME mechanism

Abstract. The mechanical behavior in liquid lead of the 15-15Ti steel coated by an alumina layer and an Alumina Forming Austenitic (AFA) steel, with a chemical composition allowing for the formation of alumina at the surface of the steel, has been studied. To investigate the liquid metal embrittlement (LME) sensitivity by liquid lead, tensile tests in air and in liquid lead have been carried out at 400 °C and 500 °C. Then analyses of the cracking and of the fracture surfaces have been performed. No LME sensitivity at the tested conditions was observed for the Al₂O₃ coated 15-15Ti steel. The AFA steel is not sensitive to LME at 400 °C but suffers from LME at 500 °C. For the AFA steel, the liquid lead promotes at 500 °C an intergranular propagation of surface cracks which suggests a grain boundary wetting-dominated LME mechanism of this steel at 500 °C.

Key words:

Tensile test

Liquid Metal Embrittlement

Fracture analysis

AFA steel

Coating

1. Introduction

One of the challenges in the development of the Lead cooled Fast Reactor (LFR) is to demonstrate the reliability of the structural materials, generally steels, in contact with the coolant, i.e. the liquid lead.

Without considering the possible irradiation damage, the life time of materials in contact with liquid metal may be reduced due to damage caused by corrosion or/and modification of the mechanical behavior in presence of liquid metal.

Indeed, corrosion by liquid metal can lead to a loss of matter, a modification of the roughness, some evolutions of the liquid metal chemistry, or changes in the material microstructure. For steels, the presence of liquid lead promotes different types of corrosion according to the oxygen content in the liquid metal, the temperature and the composition of the steels [1-2]. Indeed, at high oxygen content in liquid metal, oxidation of steels is observed. In liquid lead or liquid lead bismuth eutectic (LBE), the formation of these oxides generally limits the corrosion phenomena over time at low temperature i.e. below 500 °C. But, for the highest temperatures, because of excessive oxidation and high dissolution rates, oxide scales are not protective and other protective methods are required [1]. At low oxygen content in liquid lead or LBE, depending on the stability of the oxide of elements present in the considered steel, two effects can take place: 1. general dissolution of the steel, 2. dissolution of a selected element (in particular Ni) which can induce microstructure evolution and thus damage of the steel [1]. Therefore, to solve corrosion damage by liquid lead whatever the oxygen content issues, the presence of a protective layer at the surface of the steels has been proposed because it eliminates the contact between the steel and the liquid metal, limiting all steel / liquid metal interactions and therefore reducing the corrosion phenomena.

Though the essential challenge of the reliability of the structural materials is the corrosion resistance in liquid Pb, the mechanical resistance in liquid Pb must be ensured to guarantee the reliability of the structure under mechanical loading which is due to pure mechanical stresses or to stresses induced by temperature fluctuations. Indeed, though tough and ductile metallic alloys are selected, they may

become brittle or suffer from a loss of ductility when stressed in liquid lead and thus exhibit liquid metal embrittlement (LME) [3-8]. Two types of LME are reported: 1. LME due to a spontaneous grain boundary wetting without application of mechanical loading (for example Al/Ga or Cu/Bi couples), 2. LME which requires a critical stress resulting in prior plastic deformation. In this latter case which concerns the majority of LME systems, two conditions for LME occurrence are necessary: 1. an intimate contact between the liquid metal and the solid metal, so a good wetting of the solid metallic alloy by the liquid metal, 2. the application of plastic deformation not only at macroscopic scale but also at microscopic scale. Note that there is no particular material and metal liquid properties leading to a sensitivity to LME i.e. any metal or ductile metallic alloy may be sensitive to LME by a specific liquid metal, depending on intrinsic conditions (the microstructure of the solid metal (heat treatment, grain size, cold working, precipitations ...), the liquid metal (purity, physico-chemistry), the liquid metal / solid alloy interface (roughness, presence of native oxide at the surface of the solid alloy ...)) or experimental conditions (the temperature, the mechanical loading (monotonic, cyclic ...), the strain rate). Different studies have shown the influence of test temperature [9-14], strain rate [10, 15-16], oxygen content in liquid metal [15-18], surface roughness [19], nature of oxide layer [20], microstructure state of the steel [21-23] on the LME sensitivity of steels in contact with liquid Pb or liquid Pb-Bi. The ferritic/martensitic steels, especially the T91 steel, have been for a long time considered as promising candidates for structural materials used in contact with liquid lead or liquid LBE. But it was shown that the metallic materials with Body Centered Cubic (BCC) structure suffer from LME in lead as in LBE [1, 9, 11, 14-15, 18-19, 22-25], unlike austenitic steels such as 316L or 15-15Ti steels with a Face-Centered Cubic (FCC) structure [1, 24, 26-27]. That is why, the use of austenitic steels or FCC materials, which seem less sensitive to LME, has been favored in recent years. But because of the high Ni content, the corrosion resistance of these steels in presence of liquid lead or LBE is less important than that of ferritic/martensitic steels and is insufficient [1-2]. Therefore, to improve corrosion resistance while avoiding LME, the elaboration and characterization of austenitic steels modified to mitigate corrosion are investigated.

To mitigate corrosion of the steels in liquid lead or in liquid LBE, different solutions have been proposed and reviewed [28]. Because of its stability whatever the oxygen content in the liquid lead

and lead-bismuth eutectic, one of the most promising solutions seems to be the presence of a layer of alumina on the surface of the steel [1]. For several years, two types of options have been studied: 1. Al_2O_3 coating at the surface of the steel [29-32], 2. adapted steels, adapted metallic materials or surface treatment containing aluminum to promote the in-situ formation of a stable and protective Al_2O_3 oxide layer [18, 33-43]. The second option is based on the fact that Al is present at the bottom of the Ellingham diagram, meaning that the formation of its oxide, the alumina, is thermodynamically much more favorable and stable than the main constituting elements of the steels. Note that most of the work relates to corrosion resistance, but little to LME sensitivity [44-48].

So, the presented study concerns the mechanical behavior in liquid lead of two austenitic steels which have been modified for corrosion mitigation. In particular, it aims at evaluating if the corrosion mitigation solutions impact the LME sensitivity of these two austenitic steels: an Al_2O_3 coated 15-15Ti steel and an Alumina Forming Austenitic (AFA) steel.

The austenitic 15-15Ti steel is sensitive to corrosion by liquid lead and liquid lead alloy [33, 49]. However, no LME by LBE (with low oxygen content up to 10^{-12} wt%) was detected at 300 °C for the solution-annealed 15-15Ti steel [27]. An effect of the liquid lead was observed on creep resistance at 550 °C with a decrease of creep-rupture time, a reduction of creep strain and then the loss of steel ductility [50]. In LBE, the degradation of the creep performance of the solution-annealed 15-15Ti steel at 600 °C and 550 °C was attributed to uniform dissolution corrosion by LBE and by localized intergranular cracking [51]. But the presence of Al_2O_3 coating at the surface of the 15-15Ti steel reduces the corrosion damage due to corrosion by lead [31] and by Pb-Li [52]. Thus, the influence of the Al_2O_3 coating on the LME sensitivity of the 15-15Ti steel under monotonic loading has to be evaluated in liquid lead. This aspect already studied [53] is completed and deepened in this present work, in particular by considering welded material.

AFA steels present a good corrosion resistance, especially at high temperatures in liquid lead or LBE due to the formation of an Al rich oxide at the surface. The corrosion resistance depends, among others, on the nickel content. Indeed, it is possible to achieve excellent oxidation properties in liquid lead and to avoid dissolution attack by lowering the Ni content in AFA alloys [37]. That is why a low-Ni AFA steel (15.8% Ni) has been selected for the present study.

The influence of the presence of the liquid lead on the mechanical behavior of the Al_2O_3 coated 15-15Ti steel and the selected AFA steel has been investigated by performing tensile tests in air and in liquid lead. Then, fracture surfaces and cracking have been analyzed by scanning electron microscopy (SEM). The influences of the temperature and of the strain rate on LME sensitivity have been considered and discussed.

2. Materials and experiments

2.1. Materials

The AIM1 15Ni-15Cr Ti-stabilized steel, an austenitic stainless steel (noted 15-15Ti steel) from ENEA (Italian National Agency for New Technologies, Energy and Sustainable Economic Development) [53-54], has been delivered in the form of 3 mm thickness plates obtained by rolling. Two studied plates have been welded by TIG (Tungsten Inert Gas) (Figure 1a). The 15-15Ti steel presents an austenitic microstructure, verified by X-ray diffraction (XRD) analysis (Figure 1b), with Ti-(C,N) precipitates observed after electrolytic etching with a 60% HNO_3 and 40% H_2O solution (Figure 1c). The steel is characterized by inhomogeneous grain sizes (between 20 μm and 200 μm) of elongated shape, and by the presence of deformation marks and twins. The observed twin boundaries are most likely originated from the deformation by cold-working. The coarse and elongated Ti-(C,N) precipitates are mainly present along grain boundaries. They have mostly sizes in the range of 1-6 μm . The second type of precipitates is finer and observed at intragranular location or at twin boundaries. The hardness measured for the different directions of the plate are similar: $\text{Hv}5=305\pm 6$ (LT), $\text{Hv}5=296\pm 1$ (T), $\text{Hv}5=307\pm 5$ (L). Thus, no large differences in the hardness are observed according to the observed direction in relation to the rolling direction. The microstructure of the welded material consists of two zones (Figure 1d): 1. the fusion zone with a classic dendritic microstructure, with the directionality of the heat flow during the weld process, 2. a heat-affected zone (HAZ). In the HAZ, an austenitic microstructure with Ti-(C,N) precipitates was observed. This zone presents the same type of precipitates as observed for the base material: fine Ti-(C,N) precipitates and, elongated and coarse Ti-(C,N) precipitates. Moreover, characteristics of the austenitic grains (shape, size, presence of twins)

are similar to those of the 15-15Ti base material. The hardness of the fusion zone is equal to $Hv5=160\pm5$. That of the HAZ is similar to that of the base material.

The 15-15Ti steel has been covered by a layer of aluminum oxide using the Pulsed Laser Deposition (PLD) technique in the facilities of the Istituto Italiano di Tecnologia (IIT), Milano, Italy [30, 53, 55-56]. In PLD, a laser is used to irradiate a solid target with nano-second UV pulses, inside a vacuum chamber. The energy of the laser pulses induces a solid-vapor phase transition in the target, creating a plume of ablated particles, which expands supersonically in the vacuum chamber. The plume eventually reaches the substrate and condenses, growing the required coating [55]. The Al_2O_3 coating (Figure 1e) has an average thickness of $1.5\ \mu m$. The roughness parameter Rz , measured by optical interferometry profilometer is lower than $1\ \mu m$. No crack in the coating or at the interface between the steel and the coating was observed.

The Alumina Forming Austenitic steel, obtained by induction melting (cooling, hot rolling and annealing) was supplied by KTH (The Royal Institute of Technology in Stockholm) in the form of a bar with a diameter inferior to 10 mm and a length of about 500 mm. The obtained chemical composition as given by KTH is presented in table 1. The studied AFA steel presents an austenite microstructure, confirmed by X-ray diffraction analysis (Figure 2a). The steel, observed after etching with a 15%HF, 15% HNO_3 , 45% HCl and 25% H_2O solution, is characterized by an inhomogeneous grain size and the presence of twins, and with the presence of carbides of Nb and Ti (Figure 2b and Figure 2c). Larger precipitates with a size over $5\ \mu m$ were observed and were identified by SEM-EDX (energy dispersive X-ray spectrometer) analysis as $Ti_{0.2}Nb_{0.8}C_{0.96}$, which is confirmed by the X-Ray diffraction analysis (Figure 2a). Finer precipitates (size smaller than $1\ \mu m$) were also observed (Figure 2c). All the precipitates are located inside grains and not at grain boundaries or twin boundaries. The Vickers hardness $Hv1$ is equal to 157 ± 9 .

2.2. Experiments

Flat sample geometry was used for the tensile testing (Figure 3). The dimensions of the specimens have been defined taking into account the form and the dimensions of the available matter of each of

the two studied steels. Moreover, the dimensions of the 15-15Ti steel specimen have been defined in order to be able to carry out a test with the welded material i.e. the fusion zone, the HAZ and the base material. Concerning the 15-15Ti steel, tensile specimens have been extracted by spark machining in the two directions of the plate (noted L and T – Figure 1a) and in the welded material. Before the tensile tests of the 15-15Ti steel or before the coating process, the surfaces of the tensile specimens were mechanical polished with SiC paper up to grade 2400. Concerning the AFA steel, the tensile samples have been extracted from the 10 mm diameter bar by spark machining and no specific surface preparation has been performed.

To study the compatibility with liquid lead of the two steels, tensile tests have been performed in liquid lead but also in air for some conditions. To consider the most drastic situation for the behavior of the steel, the LME sensitivity of the Al₂O₃ coated 15-15Ti steel was evaluated in liquid lead with low oxygen content (inferior to 10⁻⁸ wt%). Indeed, a low level of oxygen in liquid LBE or liquid lead promotes the LME sensitivity by preventing or delaying the in-situ reformation of a protective oxide layer, during mechanical tests, normally responsible for limiting the interactions between the liquid metal and the studied steel [15-16]. Concerning the AFA steel, the tests were performed in oxygen saturated lead. Indeed, because the LME sensitivity is expected to be avoided in the presence of the Al₂O₃ oxide which forms instantaneously whatever the oxygen content in liquid lead, the oxygen content in the liquid metal is a less important parameter.

The used setup to test the steels in liquid lead with low oxygen content or saturated in oxygen is the one developed by Ye et al. [15] for tests in lead-bismuth eutectic with low oxygen and adapted for tensile tests in low oxygen liquid lead. It consists of two parts: 1. the purification unit for the liquid metal, 2. the mechanical test cell linked to an electro-mechanical machine to perform tensile tests in air or liquid lead. Concerning the tensile tests carried out in low oxygen liquid lead, the first step was a purification of the lead to obtain low oxygen lead. The purification unit included two melting tanks and the Ar-3.5% H₂ gas mixture as deoxygenizing agent is used. Lead ingots were molten in an external furnace and transferred to the tank 1 in the liquid state or in small solid pieces for the first step of purification. Then, after removing the superficial oxide layer under argon flow to avoid contamination of the system, the system was locked, and the preconditioning of the lead was

performed by bubbling the Ar-3.5% H_2 gas mixture through the liquid metal at a temperature between 515 °C and 535 °C, during at least 2 days. The preconditioned lead was then transferred by a tilted heating tube to the tank 2 for the second step of purification after washing the tank 2 with Ar-3.5% H_2 gas mixture. The preconditioned lead was deoxygenized by bubbling the Ar-3.5% H_2 gas mixture in the liquid metal around 520 °C in the tank 2. The oxygen content in the liquid lead was measured with a BiO/Bi sensor [57]. The purification allows decreasing the oxygen content in lead as low as 10^{-8} wt % at 520 °C. After obtention of liquid lead with sufficient low oxygen, the liquid metal was transferred at 400 °C in the mechanical test cell by a tilted heating tube. To protect the purified lead from oxidation, the interior atmosphere of the mechanical test cell was controlled thanks to a purification unit in order to remove water vapor and oxygen by flux sweeping of argon and Ar-3.5% H_2 gas, and by use of reactive filters. The oxygen content and the water content in the interior of the mechanical test cell were lowered as low as 0.1 ppm and 10 ppm respectively. The transfer of the low oxygen lead occurred at around 400-450 °C in the tank where the tensile specimen was under purified argon/hydrogen atmosphere. The tank was preheated to avoid the solidification of the liquid metal. After heating the tensile test set-up (specimen, liquid metal, set-up...) at the tensile test temperature under purified argon/hydrogen atmosphere and waiting for the stabilization of the temperature and of the displacement due to thermal expansion (1 hour), the tensile test was performed.

Concerning the tensile tests carried out in oxygen saturated liquid lead, the first step of the procedure i.e. the introduction of the lead in the tank 1, was similar. Then, without treatment by Ar/ H_2 , the liquid lead was transferred in the tank of tensile test cell, where the tensile specimen was in contact with the room atmosphere. After that, the procedure was similar as described before.

Concerning the tensile tests carried out in air, the procedure for the mechanical testing is similar but the tank of the tensile set-up is directly filled with sand.

The tensile tests were performed at two temperatures: 400 °C and 500 °C, and at two strain rates: $5 \times 10^{-5} \text{ s}^{-1}$ and $5 \times 10^{-6} \text{ s}^{-1}$. The studied temperatures correspond to those of interest for the use of the austenitic steels in the presence of liquid Pb in a Lead cooled Fast Reactor. Moreover, the strain rate of $5 \times 10^{-5} \text{ s}^{-1}$ has been the reference strain rate for several years for tensile tests in the presence of liquid LBE or liquid Pb. However, a lower strain rate has been shown to promote LME sensitivity to liquid

Pb and liquid LBE [10, 15-16] and may correspond to more realistic LFR conditions. Furthermore, the lower strain rate is preferred for tests at the highest temperature for which creep phenomena could be observed. That is why, the conditions of interest were defined as: 1. 400 °C and $5 \times 10^{-5} \text{ s}^{-1}$, 2. 500 °C and $5 \times 10^{-6} \text{ s}^{-1}$. But for the interpretation of the results and the understanding of the effect of the temperature or strain rate, additional tests have been performed at other conditions. Unless mentioned, for each condition (temperature, strain rate), two tests have been at least carried out in liquid lead. In the figures, each tensile curve represents one of the tests performed in the mentioned condition. During the tensile tests, the evolution of the force with the cross-head displacement has been recorded and the engineering stress-strain curve then determined. According to the tensile curves, the ultimate tensile strength, the yield strength, the elongation at rupture and the uniform elongation have been determined and are summarized in Table 2, Table 3, Table 4, Table 5 and Table 6. The values have not been determined for the 15-15Ti welded material with and without coating. Indeed, the welded material specimens are heterogeneous. Cracking and the fracture surfaces were analyzed by scanning electron microscope (SEM) after the test. Prior to the SEM examinations, the samples tested in liquid lead were cleaned in a solution containing CH_3COOH , H_2O_2 and $\text{C}_2\text{H}_5\text{OH}$ at a ratio of 1:1:1 to remove the solidified lead.

3. Results and discussion

3.1. Coated 15-15Ti steel

First of all, the 15-15Ti steel (base material in the direction L (rolling direction)) and the welded material without coating were evaluated in air and in presence of liquid lead to verify that the material was not sensitive to LME (Figures 4a and 4e). At 400°C and $5 \times 10^{-5} \text{ s}^{-1}$, the behavior of the 15-15Ti steel is ductile. The studied 15-15Ti steel (base material) does not present a strong strain hardening, which can be explained by the absence of heat treatment after the final cold rolling step of the steel plate. In addition, the ultimate tensile strength and the yield strength are higher than those reported in the literature for the solution-annealed 15-15Ti steel which presents a stronger strain hardening [51]. Concerning the welded material, the tensile curves present a strong strain hardening and lower stresses in comparison with the 15-15Ti steel base material (Figure 4e). This result is explained by the

microstructure of the welded material, the presence of the HAZ and is consistent with the hardness measurements. Concerning the fracture surface, a fully ductile fracture with the presence of dimples is observed in air and in liquid lead (Figures 5 and 6). No difference in the shape and in the size of the dimples was observed. The longitudinal cross-sections of the fractured welded material specimens (Figure 6) observed by SEM show the localization of the fracture in the fusion zone, the most ductile part of the welded material, and in the middle of the gauge length of the tensile specimen. Similar results in terms of tensile curves and fracture mode are obtained at 500 °C and $5 \times 10^{-6} \text{ s}^{-1}$. Thus, no LME was observed for the base material and the welded material at 400 °C and $5 \times 10^{-5} \text{ s}^{-1}$ and at 500 °C and $5 \times 10^{-6} \text{ s}^{-1}$.

To study the effect of the rolling direction, tests have been carried out for specimens extracted in the direction T (Figure 4b). As for the base material in the direction L, the base 15-15Ti steel material in the direction T presents a ductile behavior without strong strain hardening. By comparison between the tests at 400 °C and at 500 °C (Table 3), the temperature does not influence significantly the tensile curves but the stresses are more important with the decrease of the strain rate with no modification of the fracture surface. This last result is unusual but can be explained by the presence of the TiC precipitates. Comparing the results for the two directions, the values of the uniform elongation and the elongation at rupture are lower for the direction T; and the ultimate tensile strength and the yield strength higher at low strain rate (Table 2 and Table 3). As the high strength materials are generally more sensitive to LME [7, 22-23], the direction T could have led to an increased sensitivity of the material to LME. But no sign of embrittlement or of ductility loss was observed, neither on the curves, nor especially at the level of the fracture surfaces (Figure 5). Furthermore, tests carried out in liquid lead at 400 °C but at lower strain rate ($5 \times 10^{-6} \text{ s}^{-1}$) did not show LME sensitivity while a low strain rate is known to increase LME sensitivity by the liquid lead alloys of the steels. Indeed, testing at low strain rate favors the surface damage versus the volume damage and thus the effect of the damage due to the environment, in our case the liquid metal [15, 24].

The Al_2O_3 coated 15-15Ti steel has been tested in liquid lead at 400 °C and $5 \times 10^{-5} \text{ s}^{-1}$ and, at 500 °C and $5 \times 10^{-6} \text{ s}^{-1}$, and compared with the 15-15Ti steel without coating for the 3 configurations: base material in the direction L, base material in the direction T and welded material (Figures 4c, 4d, 4e).

The behavior of the coated steel is ductile and similar to the behavior of the steel without coating. But some differences in the values of stresses are noted for some conditions (Table 4 and Table 5): base material in direction L ($400\text{ }^{\circ}\text{C}$, $5\times 10^{-5}\text{ s}^{-1}$), base material in direction T ($500\text{ }^{\circ}\text{C}$, $5\times 10^{-6}\text{ s}^{-1}$). Because of the low thickness of the coating ($1.5\text{ }\mu\text{m}$) compared to the dimensions of the specimen (Figure 3), the loss of the mechanical resistance of some coated samples cannot be associated with the presence of the coating itself but is suspected to result from a modification of the steel during the coating process. Indeed, after cold forming and since the steel has not been heat treated, it contained a lot of defects (dislocations) which were recovered by the coating processes itself. Concerning the fracture mode, in all cases, the coated 15-15Ti steel presents a fully ductile fracture (Figures 7 and Figure 8). The presence of the coating induces no difference in the cracking and, in the size and shape of the dimples. For the welded material (Figure 8), the fracture is localized at the level of the fusion zone, very rarely at the interface between the fusion zone and HAZ. This does not lead to a modification of the tensile curve or to signs of embrittlement. No cracking of the Al_2O_3 coating or decohesion between the Al_2O_3 coating and the substrate was observed.

In conclusion, the results and observations that complete our previous work [53] confirm that no liquid metal embrittlement of the Al_2O_3 coated 15-15Ti steel was observed in the considered conditions.

3.2. AFA steel

Figure 9 presents the tensile tests curves obtained for the different tested conditions. Because of the scatter in the results for some conditions, all the curves are plotted. For all tested conditions, according to the tensile curves, the behavior of the studied AFA steel is ductile and presents a strong strain hardening, as expected for an annealed austenitic steel.

In air, the temperature and the strain rate do not induce any marked influence on the tensile curves (Table 6). Concerning the fracture surface after tests in air at $400\text{ }^{\circ}\text{C}$ and $500\text{ }^{\circ}\text{C}$, a ductile fracture with the presence of dimples is observed (Figures 10a and 10b). But in some cases, the fracture surface contains a large cavity, not related to the ductile fracture process (Figures 10c and 10d), and probably induced by defects due to the elaboration process. The presence of these defects explains the

scatter of the results in air. But the defects induce neither an embrittlement in air nor a significant loss of ductility or an important earlier fracture.

Concerning the tests performed at both temperatures and at $5 \times 10^{-5} \text{ s}^{-1}$, no clear influence of the presence of the liquid lead on the rupture (the ultimate tensile strength and the elongation at rupture) was noted despite a low earlier fracture (Table 6). But a scatter in the results was observed. However, a significant evolution is shown between the curves obtained in air and in liquid lead at $500 \text{ }^\circ\text{C}$ and at $5 \times 10^{-6} \text{ s}^{-1}$. Indeed, for the tests carried out in liquid lead, the fracture occurs earlier: the ultimate tensile strength, the uniform elongation and the elongation at rupture are lower.

After tests carried out in liquid lead at $400 \text{ }^\circ\text{C}$ and $5 \times 10^{-5} \text{ s}^{-1}$, a ductile fracture with the presence of dimples was observed (Figures 10e and 10f). But, for some specimens, as observed for some tests performed in air, a defect is present (Figures 10g and 10h). The morphology of this defect, i.e. a lack a matter, the ductile fracture and some local intergranular decohesion seem to indicate that the defect comes from the steel processing step and not from a liquid metal embrittlement. Indeed, because of their elongated shape in the rolling direction, these defects probably come from casting blowholes, which would not have been completely eliminated during the various hot rolling stages. The potential effect due to these elaboration defects does not seem to promote significant brittle fracture in presence of liquid lead. So, at $400 \text{ }^\circ\text{C}$ and $5 \times 10^{-5} \text{ s}^{-1}$, no LME occurs and the scatter in the tensile curves is due to some processing-generated defects present for few specimens.

For specimens tested in liquid lead at $500 \text{ }^\circ\text{C}$ and at $5 \times 10^{-5} \text{ s}^{-1}$ and $5 \times 10^{-6} \text{ s}^{-1}$, brittle and ductile fracture surfaces were observed. At $5 \times 10^{-6} \text{ s}^{-1}$, the ductile surface (Figure 11b) represents only a small part of the entire fracture surface (Figure 11). The rest of the fracture surface presents a typical intergranular brittle aspect (Figure 11c). This observation explains the early rupture observed in the tensile curves (Figure 9c). But for some samples, large decohesion of the grains was observed too (Figure 11a). The large intergranular fractured zone does not come from the elaboration process since in air it was not observed. Additionally, though $\text{Ti}_{0.2}\text{Nb}_{0.8}\text{C}_{0.96}$ precipitated inside the grains, this type of carbide was not the cause of the brittle intergranular fracture. It results therefore from the action of liquid lead i.e. a pronounced LME occurred at $500 \text{ }^\circ\text{C}$ and $5 \times 10^{-6} \text{ s}^{-1}$. LME sensitivity at $500 \text{ }^\circ\text{C}$ has been confirmed by the observations of the fracture surfaces obtained after the tests carried out in liquid lead at $500 \text{ }^\circ\text{C}$ and

$5 \times 10^{-5} \text{ s}^{-1}$. For this last condition (Figure 12), the fracture surface is ductile (Figure 12d) with the presence of dimples except for some zones near the surface of the sample, i.e. the surface in contact with the liquid metal during the tensile test (Figures 12b and 12c). The brittle surfaces are intergranular and of small area which did not impact the tensile responses (Figure 9b). But in this condition, the AFA steel suffers locally from LME by the liquid lead. However, additional tests carried out at 400°C and $5 \times 10^{-6} \text{ s}^{-1}$ in liquid lead show a ductile behavior with a fully ductile fracture surface and thus no LME (Figure 13). LME by liquid lead of the AFA steel seems to be temperature dependent.

Figures 14, 15 and 16 show the longitudinal cross-sections of the fractured samples. For the specimens tested in presence of liquid lead, there is no evident dissolution and lead penetration at the specimen surface (Figure 15d, Figure 15e, Figure 15f, Figure 16c). This is not surprising, since the duration of the tensile testing is smaller than 30 hours. Without taking into account the fracture zone due to defects coming from the elaboration (for few specimens), the specimens tested in air (Figures 14a and 15a) have a fracture surface inclined about 45° relative to the axis loading which is a sign of plastic shear deformation fracture. Concerning the specimens tested at 400°C in liquid lead, the result is similar (Figure 14b) except for the fracture zone due to the elaboration defects (Figure 14c). Numerous cracks initiated at the external surface of the specimens and propagated in the bulk could be observed after tests at 500°C in liquid lead (Figures 15b, 15c, 15d, 16a and 16b), while no obvious surface cracks are visible for the specimens tested in the other conditions i.e. in air whatever the temperature and in liquid lead at 400°C (Figures 14 and 15a). This result is not surprising for the tests in air. Indeed, in air, the ductile fracture under tensile loading is dominated by void nucleation and coalescence inside the material bulk and not by the propagation of surface cracks. The difference observed at 500°C after tests in liquid lead shows that the lead has assisted the crack propagation of the AFA steel at 500°C , but not at 400°C . The observed surface cracks propagate generally in an intergranular way (Figures 15e, 15f, 16b, 16c and 16d), which is in accordance with the fracture surface observations (Figures 11c, 12b, 12c). The $\text{Ti}_{0.2}\text{Nb}_{0.8}\text{C}_{0.96}$ carbides which are inside grains interior, are not present along the cracking path (Figures 15e, 15f, 16c, 16d).

After tests in presence of liquid lead, at 500 °C and at $5 \times 10^{-6} \text{ s}^{-1}$, lead filling into the cracks tip was observed for some cracks despite the cleaning of the samples before observations (Figure 15d). Moreover, after tests in liquid lead at 500 °C, a micrometric thickness oxide is present at the surface of the sample and at the lips of the cracks (Figures 15e, 15f and 16e). The oxide consists of the main elements of the AFA steel and of lead.

3.3. Discussion

The 15-15Ti steel base material [53] and the welded material with or without Al_2O_3 coating present a ductile behaviour in air and in liquid lead (with a low oxygen content) in the tested conditions. No liquid metal embrittlement was observed in the tested conditions despite the absence of heat treatment after cold rolling or some microstructure modifications during the elaboration of the coating. This result is explained by the significant ductility of austenitic steels which generally limits their LME sensitivity [12, 26]. However, despite their apparent immunity to LME, the steel coated with Al_2O_3 should be more deeply investigated to conclude if it is the most optimal option. Indeed, the reliability of the coated steels in presence of liquid metal could be affected by surface deterioration of the coating (cracking, wear, erosion, scaling, delamination, dissolution) in presence of liquid metal leading to a direct contact between the liquid metal and the steel. Because of the non-healing capability of the Al_2O_3 coating, the reliability of the coated 15-15Ti steel for a large duration or after a local damage or local impact could not be guaranteed.

Concerning the studied AFA steel, the tensile curves of the steel present a significant plastic domain and a strong strain hardening which could induce, as for the majority of austenitic steels or metallic alloys with a single face-centered cubic (FCC) structure, an immunity to LME by liquid lead or LBE [26-27, 58]. Moreover, despite the presence of defects resulting from the elaboration, the steel is not sensitive to LME at 400 °C, and these defects do not propagate in a brittle way due to the presence of liquid lead. This contrasts with tests at 500 °C where the AFA steel suffers from LME characterised by an intergranular fracture. Note that, because of the important ductility of the steel, the LME is partial and corresponds to a loss of ductility. The presence of liquid lead promotes at 500 °C the propagation

of cracks in an intergranular way. The effect of the liquid lead is greatest at the lowest strain rate ($5 \times 10^{-6} \text{ s}^{-1}$) which shows that a low strain rate promotes LME sensitivity. Moreover, XRD analyses carried out after tensile tests did not reveal any modification in the crystallographic feature of the steel. Thus, two parameters seem to promote the LME occurrence of the studied steel: the temperature and the strain rate. It is known that the ductility trough due to the presence of liquid metal depends on these two parameters through the existence, the depth, the bottom, the length of this ductile trough [6-8]. Moreover, the influence of these parameters depends on the mechanisms which are at the origin of LME. Thus, three different LME mechanisms [6-8] have been proposed: 1. LME explained by atomic interactions between the liquid metal and the metallic alloy, especially by adsorption and thus liquid metal-assisted interfacial cracking or liquid metal-assisted dislocation emission modification, 2. LME explained by grain boundary wetting and hence decohesion, at grain boundaries, 3. LME due to liquid metal corrosion. Except for creep, LME of steels in contact with liquid LBE or Pb is generally explained by adsorption of Pb and or Bi atoms at the surface of the steel and thus by a reduction of the steel surface energy and an adsorption-induced reduction of the bond strength, or an adsorption-induced dislocation emission modification, or simultaneous weakening induced interatomic decohesion and adsorption-induced dislocations emission modification [15-16, 19, 21, 25, 59-60]. Furthermore, for ferritic-martensitic steels with a BCC structure loaded in presence of liquid lead as liquid LBE, decreasing the strain rate is known to promote LME sensitivity [10, 15-16, 24] involving the competition of the surface damage with the bulk damage [15, 24]. For these couples, the influence of the temperature is observed through the presence of the ductility trough. Its bottom is generally located around [300 - 350 °C] and a recovery of the ductility at high temperature is observed [9-11, 13-16]. Therefore, there exists an analogy between ferritic-martensitic steels and the considered AFA steel in terms of ductility trough but not in terms of fractography. This is why the LME of the studied AFA steel does not seem to be explained by an adsorption-dominated LME mechanism. Because of the small duration of immersion of the AFA steel in liquid lead (less than 3 hours for tests carried out at 500 °C and $5 \times 10^{-5} \text{ s}^{-1}$), LME due to liquid metal corrosion could be excluded and, the LME sensitivity of the AFA steel could be attributed to a grain boundary wetting, which is known to be activated at high temperatures, while intergranular diffusion from solid metal and grain boundary

diffusion from liquid/metal occur at lower temperatures. This hypothesis is supported by the observation of the intergranular propagation of cracks at 500 °C in the presence of liquid metal. Moreover, this hypothesis is consistent with the observations of Gong et al. Indeed, Gong et al. [43] reported LME by LBE of a dual-phase Al_{0.7}CoCrFeNi (equimolar fraction) high-entropy alloy at 500 °C which is explained by the wetting of the phase boundaries between BCC and FCC phases. Thus, the wetting of grain boundaries at 500 °C by the liquid lead of the studied AFA steel could be possible especially as an intergranular crack was observed. Because the specimens have been tested without specific preparation of the surface, the initial surface of the specimens presented surface flaws. They can, as observed by Dai et al. [19], enhance the breaking of the surface oxides and thus crack initiation due to stress concentrations, thereby increasing the sensitivity to LME.

So, despite the presence of the aluminum and the possibility of oxide formation at the surface of the studied AFA steel to avoid the contact between the steel and the liquid lead, LME occurs at 500 °C.

Wetting at grain boundaries by the liquid lead seems to explain this undesirable effect for which further study is underway.

Thus, the studied AFA steel presents a ductile behavior. But despite the presence of aluminum and so the formation at the surface of an Al rich oxide, this steel suffers from a loss of ductility in presence of liquid lead and so a LME at 500 °C. Therefore, the use of this steel in presence of liquid lead seems to be limited at high temperatures. The LME was observed as a consequence of preexisting defects / flaws at the specimen surface (due to the spark machining) before testing which propagation is triggered by the liquid metal [19]. Avoiding the surface flaws at the surface could also decrease or delay the LME sensitivity and so increase the range of use of this steel in the presence of lead.

4. Conclusions

The mechanical behavior in liquid lead of a 15-15Ti steel coated by alumina layer and an Alumina Forming Austenitic (AFA) steel, selected because of the presence of alumina at the surface of the steels which should limit corrosion phenomena as liquid metal / steel interactions, has been studied.

Tensile tests in air and in liquid lead were performed at 400 °C and 500 °C, and at two strain rates: $5 \times 10^{-5} \text{ s}^{-1}$ and $5 \times 10^{-6} \text{ s}^{-1}$. The main conclusions are:

- In the tested conditions, the 15-15Ti steel with or without alumina coating presents a ductile behavior with a fully ductile fracture both in air and in liquid lead.
- No LME sensitivity to liquid lead was observed for the Al₂O₃ coated 15-15Ti steel.
- The studied AFA steel presents a ductile behavior with ductile fracture at 400 °C and 500 °C in air.
- No effect of liquid lead was observed at 400 °C.
- The AFA steel is sensitive to LME at 500 °C. The liquid lead promotes at 500 °C intergranular propagation of surface cracks. Decreasing the strain rate enhances LME sensitivity.
- The LME sensitivity at high temperature and the intergranular brittle fracture suggest a grain boundary wetting-dominated LME mechanism for this steel at 500 °C.

Both solutions chosen first to mitigate corrosion by liquid lead have been evaluated in term of LME sensitivity. If no LME sensitivity of the coated 15-15Ti steel is observed, the steel coated with Al₂O₃ could not appear as the most optimal option, because of the non-healing capability of the Al₂O₃ coating in service. But, because of its LME sensitivity, the use of the AFA steel seems to be limited at high temperatures. However, a better understanding of the phenomena and a limitation of surface flaws promoting LME initiation could possibly limit LME sensitivity of the AFA steel.

Acknowledgments.

For their participation to this study, the authors thank Damien Creton, Jocelyn Golek, Dr. Alexandre Fadel, Dr. Florent Blanchard and Yesmine Bayouhdh. Observations and analyses by SEM and XRD were performed respectively at the electron microscope facility and at the XRD platform at Lille University with the support of Chevreul Institute, the European Regional Development Fund (ERDF), and the Region Hauts-de-France (France).

Funding

This study was supported by our institutes and partially by the European Union. This research has been carried out in the frame of EERA Point Program of Nuclear Materials, funded by the European

Commission under grant agreement No. 755269, the GEMMA (Generation IV Materials Maturity) H2020 program. This work was supported by the French National Center for Scientific Research, the Lille University (France) and the National Graduate School of Engineering Chemistry of Lille (France).

References

- [1] Handbook on Lead-Bismuth Eutectic Alloy and Lead Properties, Materials Compatibility, Thermal-hydraulics and Technologies, (NEA n° 7268, OECD 2015)
- [2] C. Fazio, F. Balbaud, Corrosion phenomena induced by liquid metals in Generation IV reactors. In Structural Materials for Generation IV Nuclear Reactors (Yvon, P., Ed.; Elsevier: Amsterdam, The Netherlands, 2017)
- [3] M.H. Kamdar, Prog. Mater. Sci. 15(4) (1973) 289-374
- [4] M. Nicholas, C. Old, J. Mater. Sci. 14(1) (1979) 1-18
- [5] C.F. Old, J. Nucl. Mater. 92(1) (1980) 2-25
- [6] P.J.L. Fernandes, D.R.H. Jones, Int. Mater. Rev. 42 (1997), 251-261
- [7] B. Joseph, M. Picat, F. Barbier, Eur. Phys. J. 5 (1999) 19-31
- [8] D. G. Kolman, Corrosion 75 (2019) 42–57
- [9] J-B. Vogt, G. Nicaise, A. Legris, F. Foct, J. Phys IV 12 (2002) 217-225
- [10] J. Van den Bosch, D. Sapundjiev, A. Almazouzi, J. Nucl. Mater. 356 (2006), 237-246
- [11] F. Di Gabriele, A. Hojná, M. Chocholousek, J. Klecka, Metals 7(9) (2017) 342-356
- [12] V. Đ. Fedirko, Đ. S. Kukhar, Đ. Đ. Pohrelyuk, Kh. R. Mel'nyk, Mater. Sci. 55 (2019) 430-434
- [13] I. Proriol Serre, J.-B. Vogt, J. Nucl. Mater. (2020) 152021
- [14] X. Gong, F. Hu, J. Chen, H. Wang, H. Gong, J. Xiao; H. Wang, Y. Deng, B. Pang, X. Huang, Y. Li, Y. Yin, J. Nucl. Mater. 537 (2020) 152196
- [15] C. Ye, J-B. Vogt, I. Proriol Serre, Mater. Sci. Eng., A 608 (2014) 242-248
- [16] X. Gong, P. Marmy, B. Verlinden, M. Wevers, M. Seefeldt, Corros. Sci. 94 (2015) 377-391
- [17] M. Yurechko, C. Schroer, A. Skrypnik, O. Wedemeyer, V. Tsisar, J. Konys, J. Nucl. Mater. 512, (2018) 423-439

- [18] X. Gong, J. Chen, C. Xiang, Z. Yu, H. Gong, Y. Yin, *Corros. Sci.* 183 (2021) 109346
- [19] Y. Dai, B. Long, F. Gröschel, *J. Nucl. Mater.* 356 (2006) 222-228
- [20] T. Auger, I. Serre, G. Lorang, Z. Hamouche, D. Gorse, J.-B. Vogt, *J. Nucl. Mater.* 376 (2008) 336-340
- [21] G. Nicaise, A. Legris, J.-B. Vogt, F. Foct, *J. Nucl. Mater.* 296 (2001) 256-264
- [22] I. Serre, J.-B. Vogt, *J. Nucl. Mater.* 376 (2008) 330-335
- [23] B. Long, Z. Tong, F. Gröschel, Y. Dai, *J. Nucl. Mater.* 377 (2008) 219-224
- [24] Z. Hamouche-Hadjem, T. Auger, I. Guillot, D. Gorse, *J. Nucl. Mater.* 376 (2008) 317–321
- [25] A. Hojna, F. Di Gabriele, *J. Nucl. Mater.* (2011) 21-29
- [26] D. Gorse, T. Auger, J.B. Vogt, I. Serre, A. Weisenburger, A. Gessi, P. Agostini, C. Fazio, A. Hojna, F. Di Gabriele, J. Van Den Bosch, G. Coen, A. Almazouzi, M. Serrano, *J. Nucl. Mater.* 415 (2011) 284–292
- [27] A. Hojna, F. Di Gabriele, M. Chocholousek, Z. Spirit, L. Rozumova, *J Nucl Eng Radiat Sci* 5 (2019) 030902
- [28] J.-B. Vogt, I. Proriol Serre, *Coatings* 11 (2021) 53
- [29] P. Deloffre, F. Balbaud-Célérier, A. Terlain, *J. Nucl. Mater.* 335 (2004) 180-184
- [30] F. García Ferré, M. Ormellese, F. Di Fonzo, M.G. Beghi, *Corros. Sci.* 77 (2013) 375-378
- [31] F. García Ferré, A. Mairov, D. Iadicicco, M. Vanazzi, S. Bassini, M. Utili, M. Tarantino, M. Bragaglia, F.R. Lamastra, F. Nanni, L. Ceseracciu, Y. Serruys, P. Trocellier, L. Beck, K. Sridharan, M.G. Beghi, F. Di Fonzo, *Corros. Sci.* 124 (2017) 80–92
- [32] Z.Y. Wu, X. Zhao, Y. Liu, Y. Cai, J.Y. Li, H. Chen, Q. Wan, D. Yang, J. Tan, H.D. Liu, Y.M. Chen, J.L. Guo, J. Zhang, G.D. Zhang, Z.G. Li, B.J. Yang, *J. Nucl. Mater.* 539 (2020) 152280
- [33] G. Müller, A. Heinzl, J. Konys, G. Schumacher, A. Weisenburger, F. Zimmermann, V. Engelko, A. Rusanov, V. Markov, *J. Nucl. Mater* 335 (2004) 163-168
- [34] M. Kondo, M. Takahashi, *J. Nucl. Mater.* 356 (2006) 203-212
- [35] J. Lim, H.O. Nam, I. Hwang, K. Soon, H. Ji, *J. Nucl. Mater.* 407 (2010) 205-210
- [36] J. Lim, I. Hwang, J. Kim, *J. Nucl. Mater.* 441 (2013) 650-660
- [37] J. Ejenstam, P. Szakálos, *J. Nucl. Mater.* 461 (2015) 164-170

- [38] M. Roy, L. Martinelli, K Ginestar, J. Favergeon, G. Moulin, J. Nucl. Mater. 468 (2016) 153-163
- [39] P. Dömstedt, M. Lundberg, P. Szakalos, Oxid. Met. 91 (2019) 511-524
- [40] H. Shi, A. Jianu, A. Weisenburger, C. Tang, A. Heinzl, R. Fetzer, F. Lang, R. Stieglitz, G. Müller, J. Nucl. Mater. 524 (2019) 177-190
- [41] H. Wang, H. Yu, S. Kondo, N. Okubo, R. Kasada, Corros. Sci. 175 (2020), 108864
- [42] H. Shi, R. Fetzer, A. Jianu, A. Weisenburger, A. Heinzl, F. Lang, G. Müller, Corros. Sci. 190 (2021) 109659
- [43] X. Gong, C. Xiang, T. Auger; J. Chen, X. Liang, Z. Yu, M.P Short, M. Song, Y. Yin, Script. Mater. 194 (2021) 113652
- [44] A. Weisenburger, A. Heinzl, C. Fazio, G. Müller, V.G. Markow, A.D. Kastanov, J. Nucl. Mater. 377 (2008) 261–267
- [45] I. Proriol Serre, I. Diop, N. David, M. Vilasi, J.-B. Vogt, Surf. Coat. Technol. 205 (2011) 4521-4527
- [46] E. Yamaki, M. Takahashi, J. Nucl. Sci. Technol. 48 (2011) 797–804
- [47] E. Yamaki-Irisawa, S. Numata, M. Takahashi, Prog. Nucl. Energy 53 (2011) 1066–1072
- [48] A. Weisenburger, A. Jianu, W; An, R. Fetzer, M. Del Giacco, A. Heinzl, J. Nucl. Mater. 431 (2012) 77–84
- [49] A. Heinzl, A. Weisenburger, G. Müller, J. Nucl. Mater. 448 (2014) 163–171
- [50] A. Strafella, A. Coglitore, P. Fabbri, E. Salernitano, Frattura ed Integrità Strutturale, 42 (2017) 352-365
- [51] X. Gong, Z. Yang, Y. Deng, J. Xiao, H. Wang, Z. Yu, Y. Yin, Mater. Sci. Eng., A 798 (2020) 140230
- [52] D. Iadicicco, M. Vanazzi, F. García Ferré, B. Paladino, S. Bassini, M. Utili, F. Di Fonzo, Fus. Eng. Des. 146 (2019) 1628–1632
- [53] I. Proriol Serre, I. Ponsot, J.-B. Vogt, MATEC Web of Conference 349 (2021) 02007
- [54] G. Barbieri, F. Cognini, L. Pilloni, D. Mirabile Gattia, C Daniele, Mater. Sci. Forum 1016 (2021) 262-267
- [55] J. Schou, Appl. Surf. Sci. 255 (2009) 5191-5198

- [56] F. Di Fonzo, D. Tonini, A. Li Bassi, C. Casari, M. Beghi, C. Bottani, D. Gastaldi, P. Vena, R. Contro, Appl. Phys. A 93 (2008) 765-769
- [57] J-L. Courouau, J. Nucl. Mater. 335 (2004), 254-259
- [58] X. Huang, X. Gong, M. Song, J. Chen, F. Hu, Y. Yin, J. Xiao, H. Wang, H. Wang, H. Gong, Y. Yangbin Deng, B. Pang, Y. Li, J Nucl. Mater. 528 (2020) 151859
- [59] T. Auger, G. Lorang, Scripta Mater. 52(12) (2005) 1323-1328
- [60] X. Gong, P. Marmy, A. Volodin, B. Amin-Ahmadi, L. Qin, D. Schryvers, S. Gavrilov, E. Stergar, B. Verlinden, M. Wevers, M. Seefeldt, Corros. Sci. 102 (2016) 137-152

Tables

Table 1: Chemical composition of the used AFA steel in wt %.

Element	Al	Cr	Ni	Mn	C	Nb	Ti	Cu	Fe
wt %	2.7	12	15.8	3.5	0.07	1	0.2	2.5	Bal

Table 2: The ultimate tensile strength, the yield strength, the elongation at rupture and the uniform elongation determined according to the tensile curves for the 15-15Ti steel (direction L).

	Ultimate tensile strength (MPa)	Yield strength (MPa)	Elongation at rupture (%)	Uniform elongation (%)
400 °C/5×10 ⁻⁵ s ⁻¹ /air	731	650	16.8	10.4
400 °C/5×10 ⁻⁵ s ⁻¹ /lead	763 ± 0	675 ± 7	16.8 ± 0.3	11.6 ± 1.2
500 °C/5×10 ⁻⁶ s ⁻¹ /lead	724 ± 31	615 ± 21	16.6 ± 0.1	12.6 ± 0

Table 3: The ultimate tensile strength, the yield strength, the elongation at rupture and the uniform elongation determined according to the tensile curves for the 15-15Ti steel (direction T).

	Ultimate tensile strength (MPa)	Yield strength (MPa)	Elongation at rupture (%)	Uniform elongation (%)
400 °C/5×10 ⁻⁵ s ⁻¹ /air	773	700	14.2	9.8
400 °C/5×10 ⁻⁵ s ⁻¹ /lead	773 ± 4	705 ± 7	12.5 ± 1.4	7.3 ± 0.4
400 °C/5×10 ⁻⁶ s ⁻¹ /lead	885 ± 28	803 ± 18	12.8 ± 1.8	9.2 ± 1.1
500 °C/5×10 ⁻⁶ s ⁻¹ /lead	886 ± 37	775 ± 21	14.6 ± 0.18	10.4 ± 0.14

Table 4: The ultimate tensile strength, the yield strength, the elongation at rupture and the uniform elongation determined according to the tensile curves for the coated 15-15Ti steel (direction L).

	Ultimate tensile strength (MPa)	Yield strength (MPa)	Elongation at rupture (%)	Uniform elongation (%)
400 °C/5×10 ⁻⁵ s ⁻¹ /lead	701 ± 2	633 ± 4	12.7 ± 0.6	8.5 ± 0.7
500 °C/5×10 ⁻⁶ s ⁻¹ /lead	736 ± 15	627 ± 23	14.7 ± 1.5	11.5 ± 2.3

Table 5: The ultimate tensile strength, the yield strength, the elongation at rupture and the uniform elongation determined according to the tensile curves for the coated 15-15Ti steel (direction T).

	Ultimate tensile strength (MPa)	Yield strength (MPa)	Elongation at rupture (%)	Uniform elongation (%)
400 °C/5×10 ⁻⁵ s ⁻¹ /lead	769 ± 63	698 ± 40	11.6 ± 0.7	7.5 ± 0.6
500 °C/5×10 ⁻⁶ s ⁻¹ /lead	732 ± 6	625 ± 21	12 ± 0.2	8.7 ± 0.9

Table 6: The ultimate tensile strength, the yield strength, the elongation at rupture and the uniform elongation determined according to the tensile curves for the AFA steel.

	Ultimate tensile strength (MPa)	Yield strength (MPa)	Elongation at rupture (%)	Uniform elongation (%)
400 °C/5×10 ⁻⁵ s ⁻¹ /air	490 ± 39	162 ± 4	40.7 ± 2.2	40 ± 0.5
400 °C/5×10 ⁻⁵ s ⁻¹ /lead	511 ± 18	153 ± 13	40.8 ± 7.4	46.5 ± 2.12
500 °C/5×10 ⁻⁵ s ⁻¹ /air	521 ± 15	190 ± 14	43.9 ± 5.9	42.3 ± 4.9
500 °C/5×10 ⁻⁵ s ⁻¹ /lead	467 ± 5	158 ± 4	40.5 ± 3.5	40.1 ± 4.2
500 °C/5×10 ⁻⁶ s ⁻¹ /air	546 ± 16	175 ± 21	52 ± 1.4	50 ± 2.8
500 °C/5×10 ⁻⁶ s ⁻¹ /lead	390 ± 20	160 ± 0	19.9 ± 4.2	17.5 ± 0.7

Figures

Figure 1: a): Schematic of TIG welded 15-15Ti plate, b) XRD diffractogram with phase identification, c): SEM micrograph of the base material (face L), d): SEM micrograph of the welding material and e): cross section of the coated 15-15Ti steel.

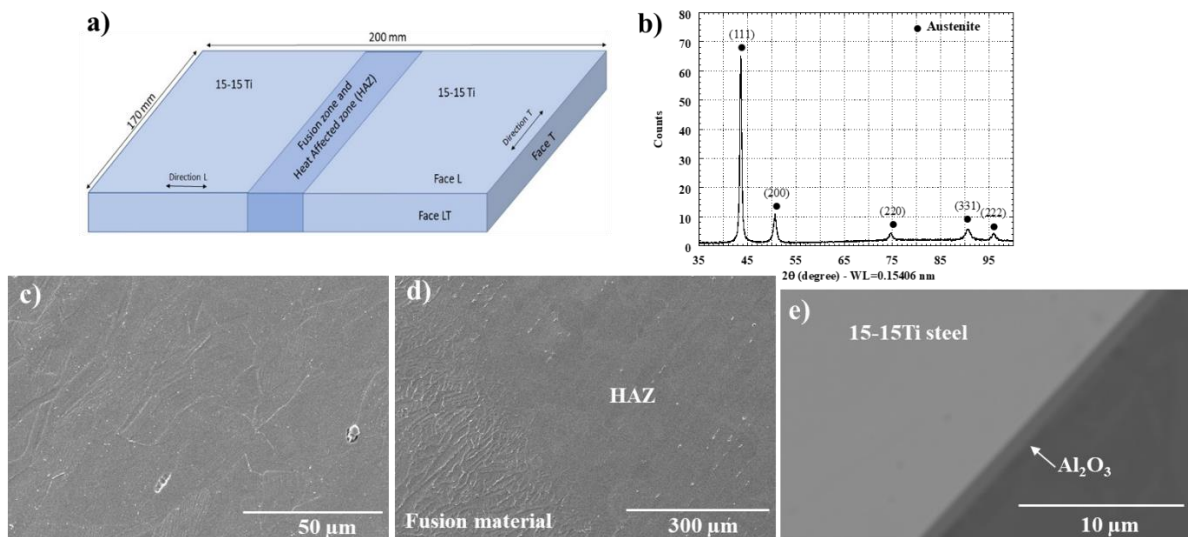


Figure 2: a): XRD diffractogram with phase identification - b) and c): SEM micrograph of the studied AFA steel (arrows pointing to some fine precipitates).

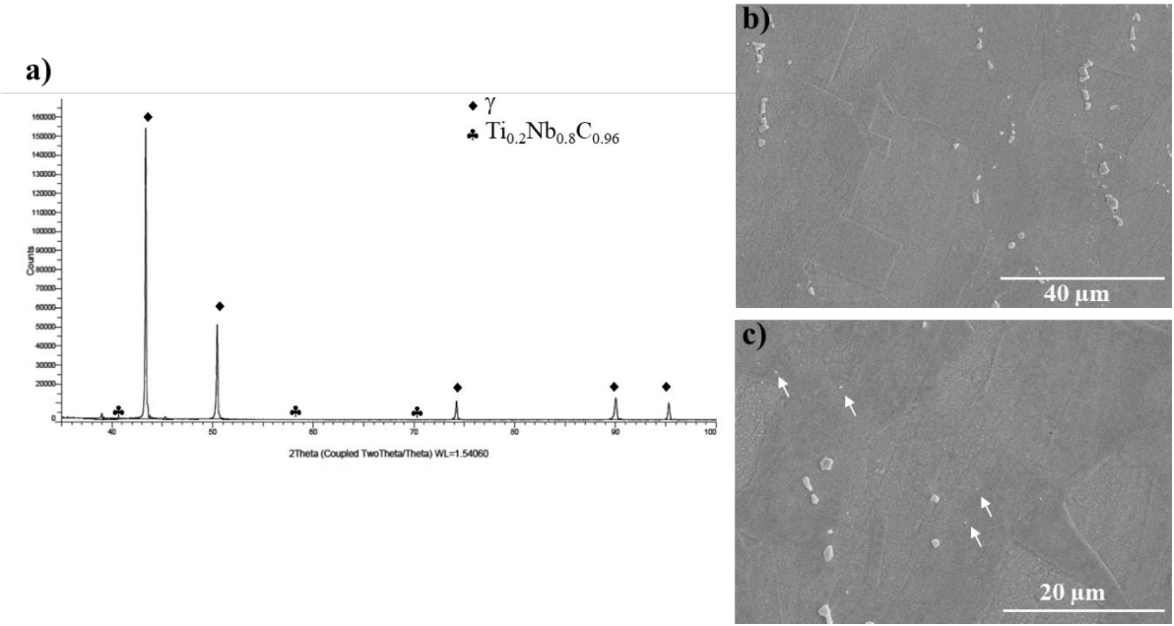


Figure 3: drawing of tensile specimens (measurements in mm).

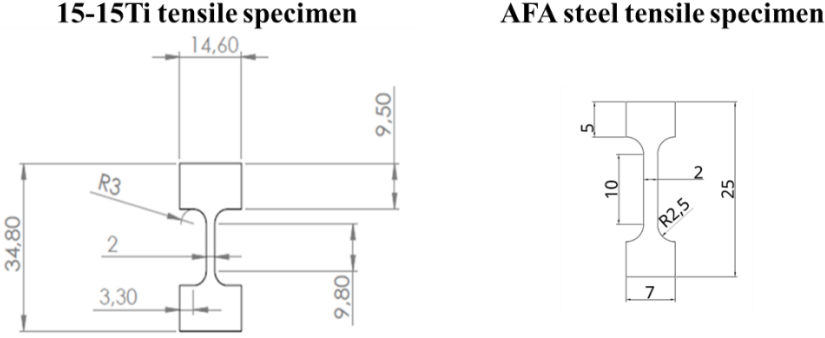


Figure 4: engineering stress-strain curves of 15-15Ti steel: a): base material in direction L without coating, b): base material in direction T without coating, c): coated base material in direction L, d): coated base material in direction T, e): welded material with and without coating.

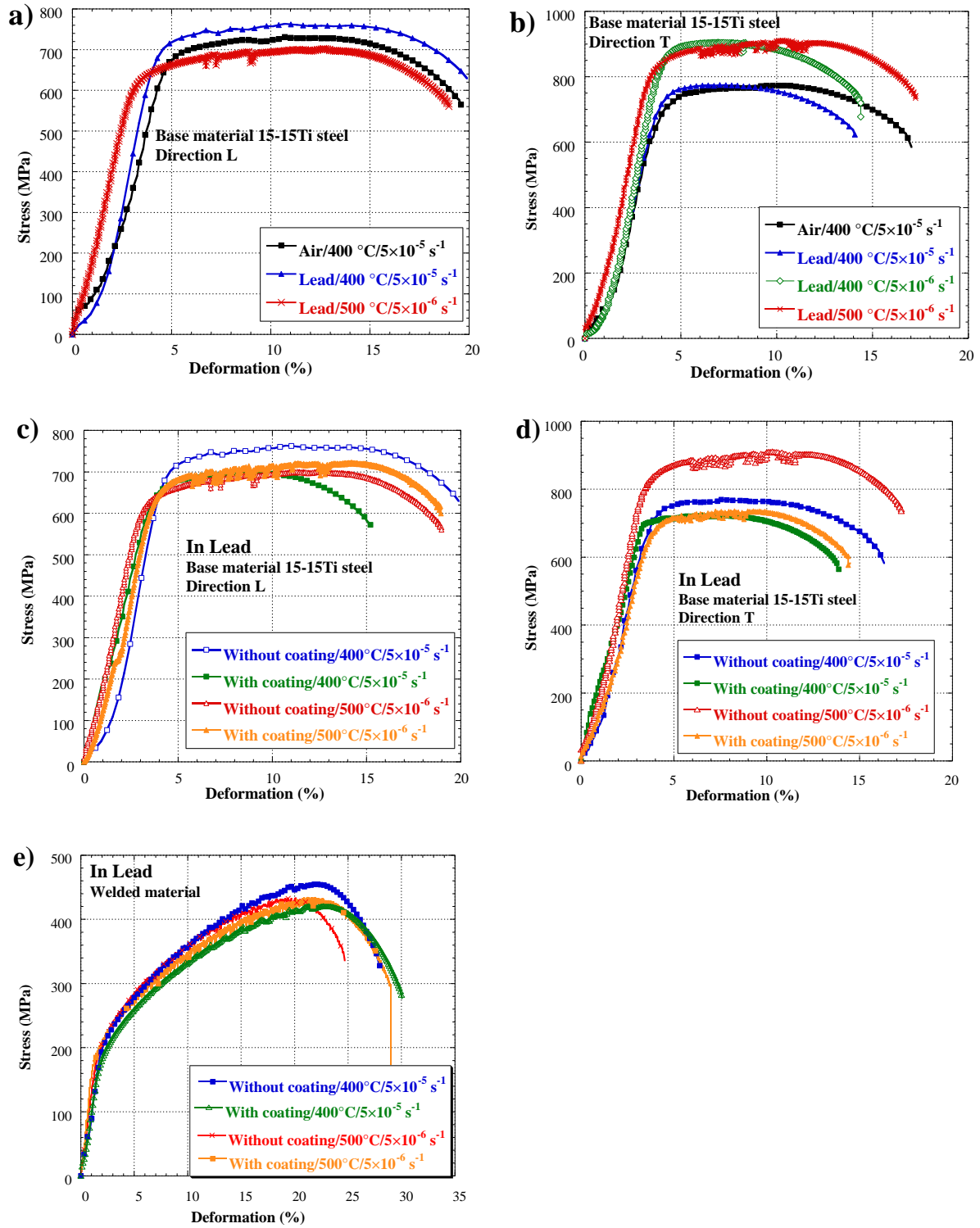


Figure 5: fracture surfaces after tests at 400 °C and at $5 \times 10^{-5} \text{ s}^{-1}$ in low oxygen lead of 15-15Ti steel without coating (from left to right: overview, in the center, at the edge): a), b) and c): base material in direction L, d), e) and f): base material in direction T.

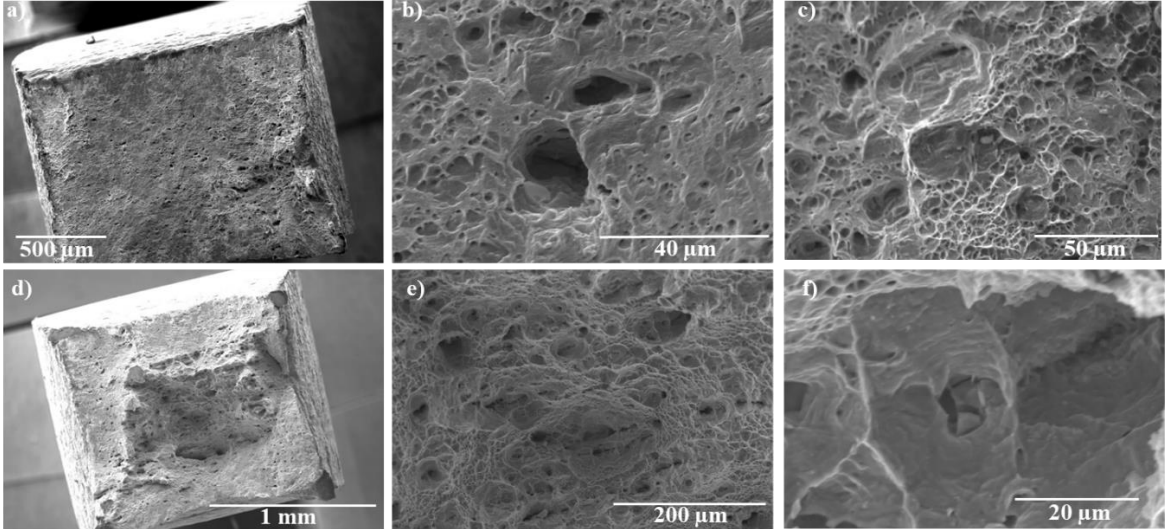


Figure 6: welded material without coating tested in low oxygen lead at 500 °C and at $5 \times 10^{-6} \text{ s}^{-1}$: a), b), c): fracture surface: a): overview, b): in the center, c): at the edge, d): cross-section of the fractured sample.

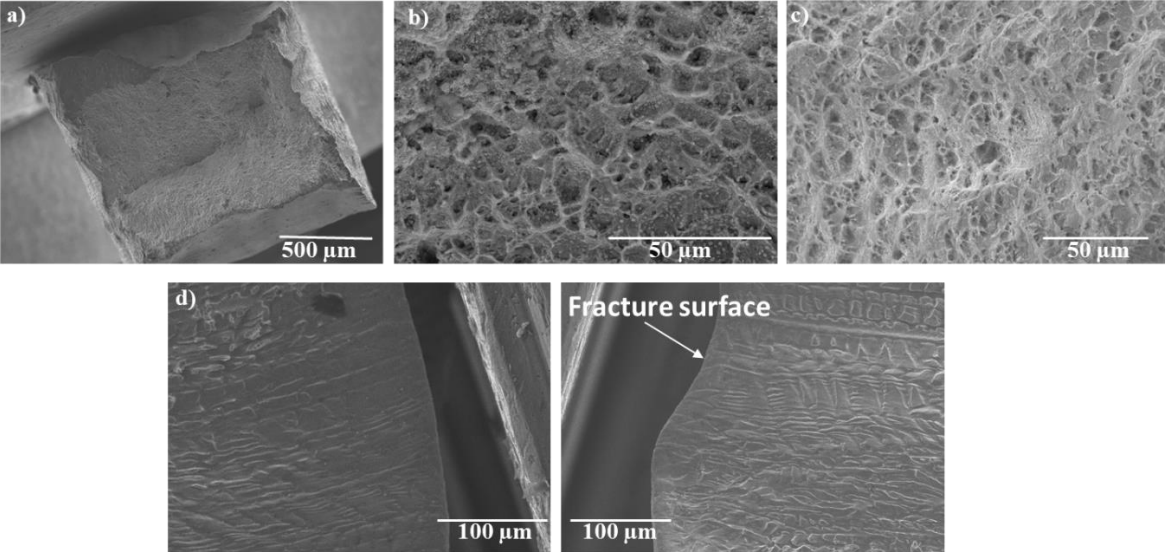


Figure 7: fracture surfaces after tests in low oxygen lead of coated 15-15Ti steel (from left to right: overview, in the center, at the edge): a), b) and c): base material in direction L at 400 °C and at $5 \times 10^{-5} \text{ s}^{-1}$, d), e) and f): base material in direction T at 500 °C and at $5 \times 10^{-6} \text{ s}^{-1}$.

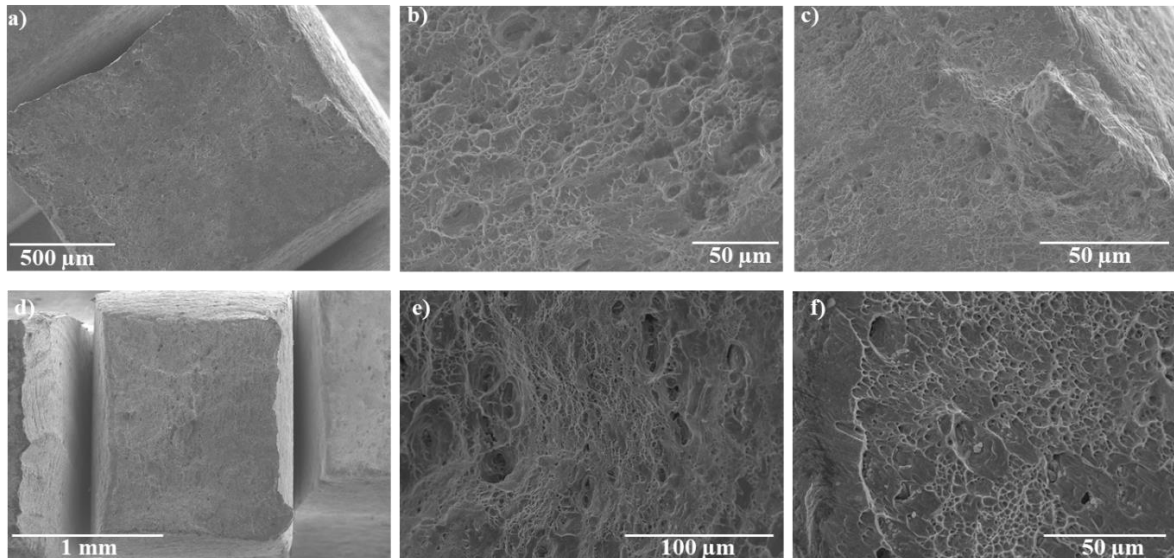


Figure 8: coated welded material tested in low oxygen lead at 400 °C and at $5 \times 10^{-5} \text{ s}^{-1}$: a), b), c): fracture surface: a): overview, b): in the center, c): at the edge, d): cross-section of the fractured sample.

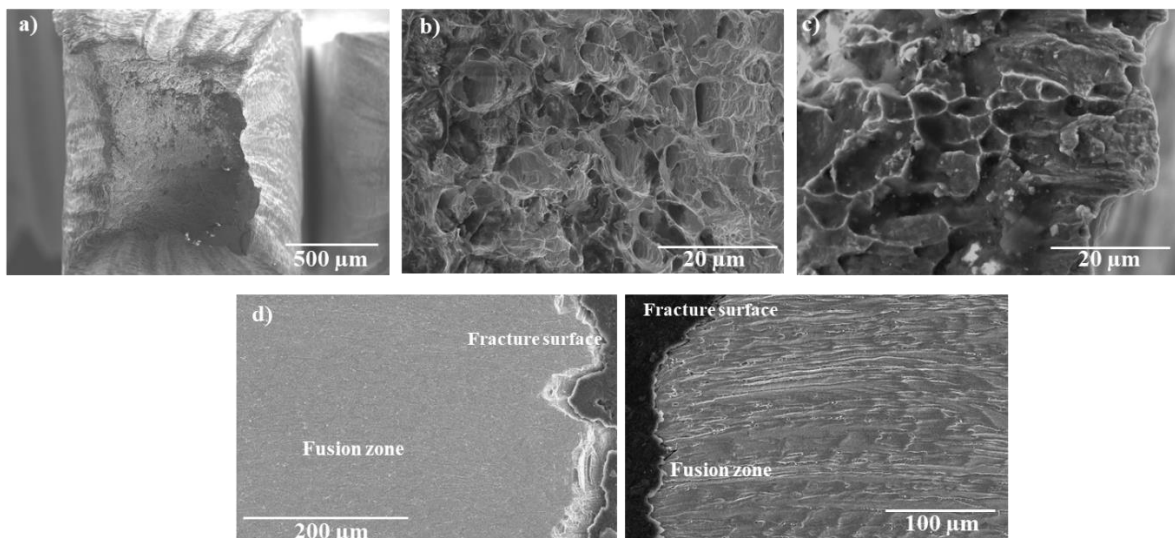


Figure 9: engineering stress-strain curves of the AFA steel obtained in air and in oxygen saturated lead: a): at 400 °C and at $5 \times 10^{-5} \text{ s}^{-1}$, b): at 500 °C and at $5 \times 10^{-5} \text{ s}^{-1}$, c): at 500 °C and at $5 \times 10^{-6} \text{ s}^{-1}$.

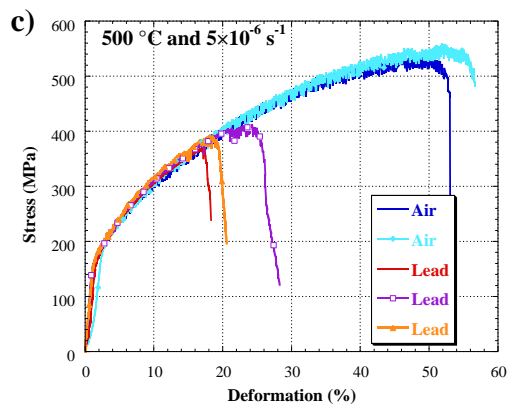
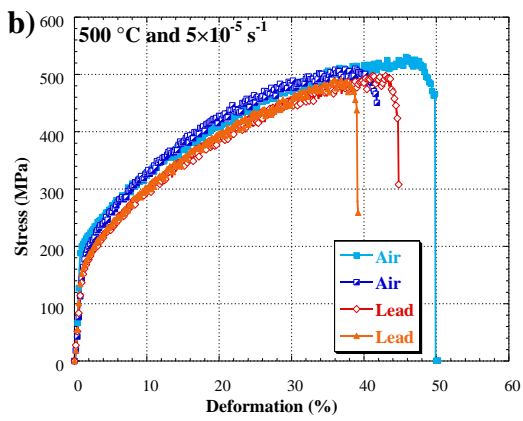
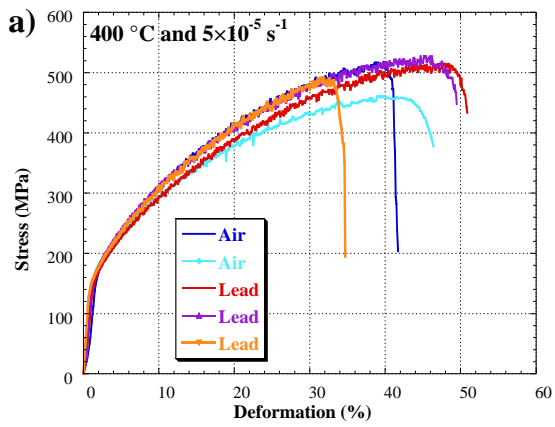


Figure 10: fracture surfaces of the AFA steel after tests at 400 °C and at $5 \times 10^{-5} \text{ s}^{-1}$; in air: a) and c): overview, b): ductile fracture near the edge of the surface, d): default of the material with local embrittlement and ductile fracture ; in presence of liquid lead: e) and g): overview, f): ductile fracture near the edge of the surface, h): default of the material with local embrittlement and ductile fracture.

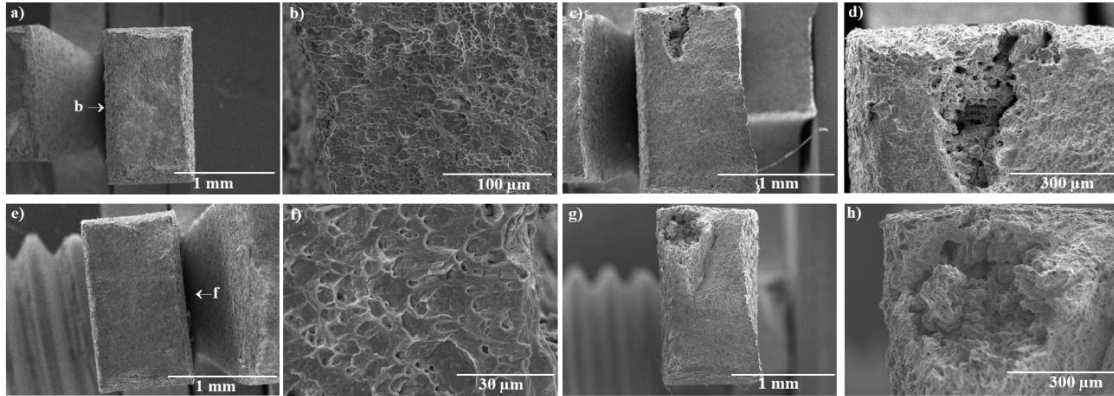


Figure 11: fracture surface of the AFA steel after test at 500 °C and at $5 \times 10^{-6} \text{ s}^{-1}$ in presence of liquid lead: a): overview, b): ductile fracture, c): brittle intergranular fracture.

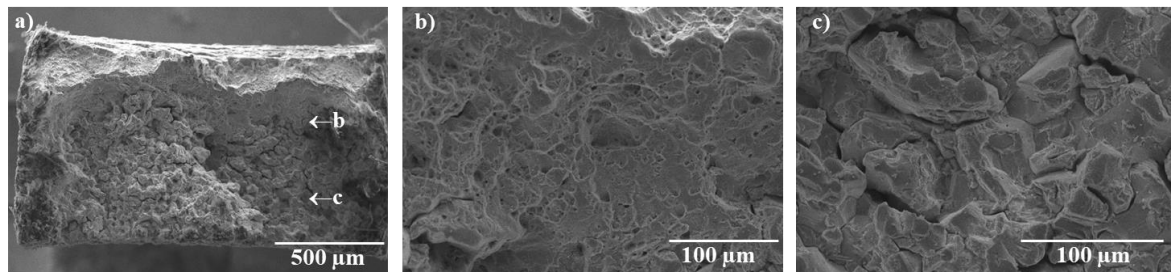


Figure 12: fracture surface of the AFA steel after test at 500 °C and at $5 \times 10^{-5} \text{ s}^{-1}$ in presence of liquid lead: a): overview, b) and c): brittle intergranular fracture near the edge of the surface, d): ductile fracture.

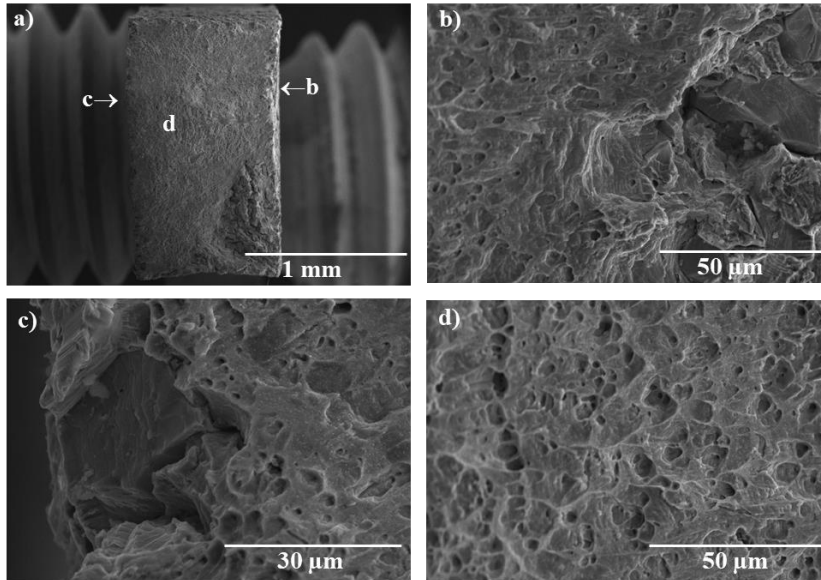


Figure 13: fracture surface of the AFA steel after test at 400 °C and at $5 \times 10^{-6} \text{ s}^{-1}$ in presence of liquid lead: a): overview, b) and c): ductile fracture near the edge of the surface.

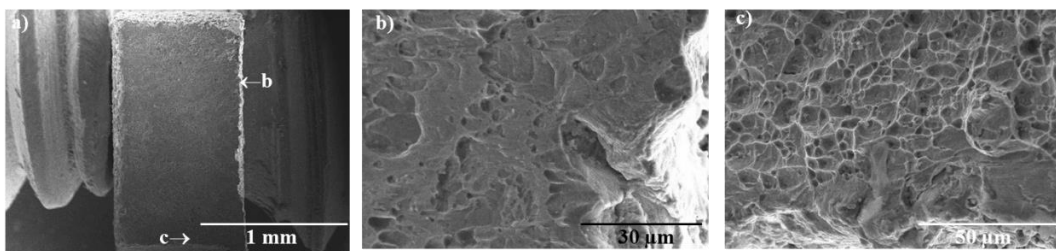


Figure 14: longitudinal cross-sections of the AFA steel fractured at 400 °C and at $5 \times 10^{-5} \text{ s}^{-1}$ in air and in presence of liquid lead: macroscopic view.

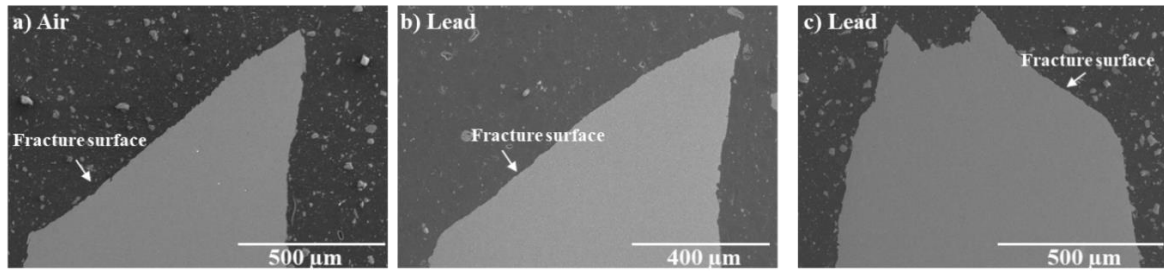


Figure 15: longitudinal cross-sections of the AFA steel fractured at 500 °C and at $5 \times 10^{-6} \text{ s}^{-1}$ in air and in presence of liquid lead: a), b) and c): macroscopic view, d), e) and f): secondary cracks.

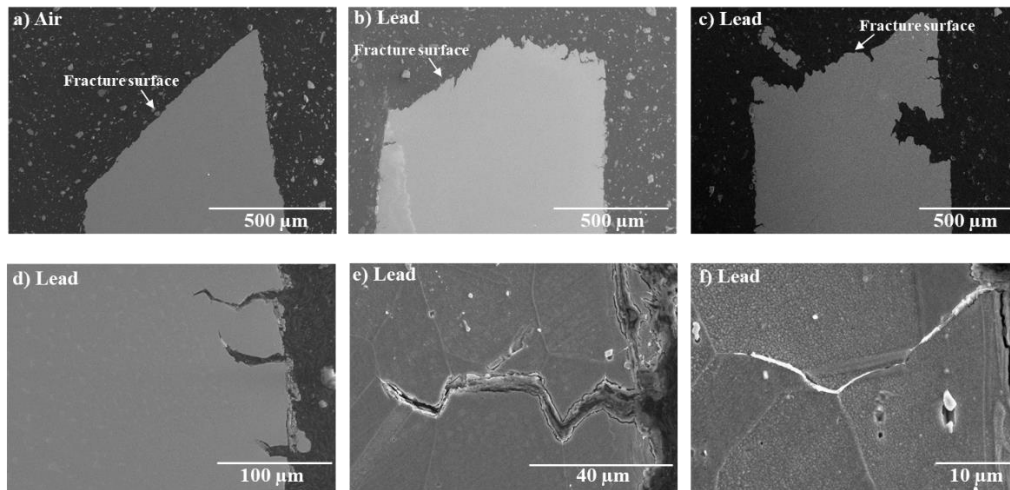


Figure 16: longitudinal cross-sections of the AFA steel fractured at 500 °C and at $5 \times 10^{-5} \text{ s}^{-1}$ in presence of liquid lead: a): macroscopic view, b), c) and d): secondary cracks, e): details of the crack tip of the image d).

